frontiers | Frontiers in Earth Science

TYPE Original Research
PUBLISHED 29 April 2025
DOI 10.3389/feart.2025.1452399

Check for updates

OPEN ACCESS

EDITED BY
Nibir Mandal,
Jadavpur University, India

REVIEWED BY
Dip Ghosh,
University of Calcutta, India
Ajay Kumar,
Indian Institute of Science Education and Research, Pune, India

*CORRESPONDENCE
A. Baranov,
aabaranov@gmail.com

RECEIVED 20 June 2024
ACCEPTED 14 April 2025
PUBLISHED 29 April 2025

CITATION
Baranov A, Bobrov A, Tenzer R and Chuvaev A (2025) Evolution of lateral tectonophysical stresses in the spherical shell convection with an immobile supercontinent.
Front. Earth Sci. 13:1452399.
doi: 10.3389/feart.2025.1452399

Evolution of lateral tectonophysical stresses in the spherical shell convection with an immobile supercontinent

A. Baranov[1]*, A. Bobrov[2], R. Tenzer[1] and A. Chuvaev[1]

[1]Department of Land Surveying and Geo-Informatics, Hong Kong Polytechnic University, Kowloon, Hong Kong SAR, China, [2]Laboratory of Geomechanics, Schmidt Institute of Physics of the Earth of the Russian Academy of Sciences, Moscow, Russia

We investigate the evolution of horizontal stress field after implementing a supercontinent into spherical mantle model with phase transitions, the temperature- and pressure-dependent rheology, while assuming that the mantle is heated from the base and from within. Before implementation of the supercontinent, the overlithostatic horizontal stresses in the areas of mantle upwellings/downwellings are about ±25 MPa and more, whereas for the rest upper mantle horizontal stresses are in the range of ±15 MPa. The supercontinent covered one-third of the Earth`s surface and it is modeled as an undeformable, highly viscous immobile lid with respect to the ambient mantle and it is abruptly imposed on well-developed mantle convection. The area of supercontinent is limited by a spherical angle ($\theta \le 66.4°$). After implementation, the mantle flow is rearranged and a group of upwelling mantle flows is formed under the supercontinent and their hot heads increase in size due to the heat-insulating effect of the supercontinent, while quasi-linear subduction zones increase in the oceanic regions. As a result, the average temperature of the area under the supercontinent rises over time and becomes higher than the average temperature of the suboceanic area, where cold descending mantle flows intensify. At the depth covering the interval from 300 to 400 km under the supercontinent the temperature rises on average by 60 K. Formed under the supercontinent, upwelling mantle flows dramatically change the stress pattern in the supercontinental area producing tensional stresses in the supercontinent and overlithostatic compressive horizontal stresses in the subcontinent mantle. Tensile overlithostatic horizontal stresses inside the supercontinent change from 25 to 50 MPa in different continental areas, whereas beneath the supercontinent the overlithostatic compressive horizontal stresses in the subcontinent mantle are about 20–60 MPa. Only for the model with weak zone around the supercontinent stresses can reach 100 MPa.

KEYWORDS

supercontinent, spherical mantle convection, thermal insulating, horizontal stresses, spherical convection

1 Introduction

Geological and palaeo-magnetic evidence suggests the formation of several supercontinents during the Earth's history (e.g., Rogers, 1996; Meert, 2002; Zhao et al., 2004; Rogers and Santosh, 2009; Piper, 2010; Pesonen et al., 2012; Zhang et al., 2012; Nance et al., 2014; Mitchell et al., 2021). The relationship between the supercontinent cycle and various geological and tectonic events have been investigated in numerous studies, such as orogenic formations (Hoffman, 1991), sea level variations (Anderson, 1982), and flood basalt volcanism (Courtillot and Renne, 2003; Condie, 2004). The effect of a super-continent cycle on the climate was studied by Donnadieu et al. (2004), Rogers and Santosh (2004), Nance et al. (2014) and others.

The influence of supercontinents on 3D mantle convection has been investigated numerically, for instance, by Lowman and Gable (1999), Yoshida et al. (1999), Honda et al. (2000), Phillips and Bunge (2005), Phillips and Bunge (2007), Zhong et al. (2007), Li and Zhong (2009), Yoshida (2010), Heron and Lowman (2011), Yoshida (2013), Yoshida (2019), Lobkovsky and Kotelkin (2015), Zhang et al. (2018), Mao et al. (2019), Yoshida (2019), and others. These studies revealed that, due to the influence of the supercontinent, the mantle flow is rearranged and a group of mantle plumes appears under the supercontinent after some time. Nevertheless, the stress variations with depth from the lithosphere to lower mantle are still poorly understood. At the same time, tensile stresses in the supercontinent are connected with stresses in the surrounding mantle and show in what state it is at the current stage.

The studies where stresses during the supercontinent cycle were investigated are presented in Table 1. Tensional stresses in the supercontinent change in a rather wide range from 30 MPa (Yoshida, 2010) to about 100 MPa (Yoshida, 2019) or even 200 MPa (Bobrov and Baranov, 2019; Bobrov et al., 2022). For spherical models, the stresses were calculated, for example, by Yoshida (2010), Huang et al. (2019) and Yoshida (2019). The magnitude of critical stresses required for a supercontinent to disintegrate depends on the model and rheology of the mantle as well as how the supercontinent is constructed. In studies where the self-consistent supercontinent formation model is used, this leads to the inherited heterogeneities (e.g., previous orogens) allowing for the localization of deformation under tensile stresses.

Despite numerous studies investigated convection in the mantle and the lithosphere, the stress evolution in time and space is not yet fully understood, particularly the evolution of stresses in the supercontinent. We address this aspect here by investigating the stresses in the supercontinent and in the mantle, while adopting a 3-D spherical model with the pressure- and temperature-dependent viscosity and phase transitions. In our calculations, the immobile supercontinent is modeled as an undeformable area with a high viscosity (1,000 units in non-dimensional form, here 1 unit is taken equal to 0.5 × 10^{22} Pa s). The supercontinent is implemented instantaneously on a well-developed mantle convection pattern.

Below we present a brief overview of theoretical and numerical models. The results of numerical modeling are presented in Section 3 and discussed in Section 4. The study is concluded in Section 5.

2 Numerical model setup

2.1 Theoretical model and governing equations

We modeled the Earth's mantle as the Boussinesq fluid with the infinite Prandtl number in a 3D spherical geometry. The mantle is heated from the core and from within by decay of radioactive elements (internal heating). In our model for spherical mantle convection, the dimensionless equations for conservation of mass, momentum, and energy read (e.g., McNamara and Zhong, 2004; Zhong et al., 2007; Bobrov and Baranov, 2014; Bobrov and Baranov, 2016; Bobrov and Baranov, 2018):

$$\nabla \cdot \mathbf{v} = 0 \tag{1}$$

$$-\nabla p + \nabla \cdot \tau = \left(-\mathrm{RaT} + \mathrm{Ra}_{ph410}\Gamma_{410} + \mathrm{Ra}_{ph660}\Gamma_{660}\right)\mathbf{e}_r \tag{2}$$

$$\partial T/\partial t + \mathbf{v} \cdot \nabla T = \nabla^2 T + H, \tag{3}$$

where $\mathbf{v}$ is the velocity vector; p is the dynamic pressure; τ is the deviatoric tensor of viscous stresses; T is the temperature; t is the time, Γ is the phase function; $\mathbf{e}_r$ is the unit vector in the radial direction, H is the internal heat production; Ra is the thermal Rayleigh number; and Ra_{ph} is the phase Rayleigh number. The non-dimensional parameters are the thermal Rayleigh number $\mathrm{Ra} = \alpha\frac{\rho g \Delta T R^3}{\kappa\eta_0}$, the phase Rayleigh number $\mathrm{Ra}_{ph} = \frac{\Delta\rho g R^3}{\kappa\eta_0}$, and the internal heat production number H. In addition, we defined the following parameters (Table 2): the thermal expansivity $\alpha = 2 \times 10^{-5}\ \mathrm{K}^{-1}$, the density $\rho = 4{,}600\ \mathrm{kg\ m}^{-3}$, the gravitational acceleration $g = 9.8\ \mathrm{ms}^{-2}$, the super-adiabatic temperature drop ΔT = 2500° between the core-mantle boundary and the surface, the Earth's radius R = 6371 km, the radius of the Earth's core R_{core} = 3471 km (dimensionless 0.5448), the reference viscosity $\eta_0 = 0.5 \times 10^{22}$ Pa s, and the thermal diffusivity $\kappa = 10^{-6}\ \mathrm{m}^2\ \mathrm{s}^{-1}$. The density contrasts $\Delta\rho$ on phase borders were set up as follows: $\Delta\rho_{410} = 0.07$, $\Delta\rho_{660} = 0.09$; $\gamma_{410} = 1.6$ MPa/K; $\gamma_{660} = -1.3$ MPa/K (Fei et al., 2004).

According to the parameters summarized in the preceding paragraph, $Ra = 1.2 \times 10^8$ and the phase Rayleigh numbers at the depth of 410 and 660 km are $Ra_{ph410} = 1.68 \times 10^8$ and $Ra_{ph660} = 2.16 \times 10^8$. H in our base model (model 1) was set to be 120 to yield a 60%–70% internal heat (Leng and Zhong, 2009; Zhang et al., 2018).

The scaling factors for the variables in Equations 1–3 are: R for the length, R^2/κ for the time, κ/R for the velocity, and $\kappa\,\eta_0/R^2$ for the pressure p and τ. The free-slip, impermeable, and isothermal boundary conditions are applied at the top and bottom (core-mantle) boundaries of the mantle with values of $T_{top} = 0$ and $T_{bottom} = 1$, respectively.

The horizontal overlithostatic stress, in particular lateral normal stresses $\sigma_{\theta\theta}$, which are oriented along the surface, and directed along the change in latitude θ,is defined by (Schubert et al., 2001):

$$\sigma_{\theta\theta} = \tau_{\theta\theta} - p, \tag{4}$$

where

$$\tau_{\theta\theta} = 2\eta\left(\frac{1}{r}\frac{\partial V_\theta}{\partial\theta} + \frac{V_r}{r}\right). \tag{5}$$

TABLE 1 Studies investigating stresses in the supercontinent.

No	Paper	Type of model	Stresses	Supercontinent cycle
1	Gurnis (1988)	2-D isoviscous models (aspect ratio is 1:8) with periodic boundary conditions, Ra = 1 × 10^5; the continents were modelled as nondeformable Cartesian rectangles on the surface with high viscosity and low density	The tensile yield stress was set at 50–70 MPa, the variation in the horizontal stresses 10–100 MPa	Full cycle, two continents
2	Lowman and Jarvis (1993)	2D Cartesian models (1:4) with Ra = 1.2 × 10^5 and internal heating. Rigid continents are floating on the isoviscous mantle	The tensile yield stress was set at 48 MPa	Incomplete cycle, two continents
3	Lowman and Jarvis (1996)	2-D Cartesian models (1:4) with Ra = 1 × 10^7 and internal heating. Rigid continents are floating on the isoviscous mantle	The tensile yield stress was set at 80 MPa	Incomplete cycle, two continents
4	Lowman and Jarvis (1999)	2-D Cartesian models (1:8) with Ra = 1 × 10^7 for whole mantle model with different internal heating. Rigid continents are floating on the isoviscous mantle	The tensile yield stress was set at 80 MPa	Incomplete cycle, two continents before collision and three after supercontinent breakup
5	Butler and Jarvis (2004)	Spherical annulus (2-D), Ra = 1.12 × 10^7, immobile supercontinent modeled by a high-viscosity region (at a North Pole and equator)	Tensional stresses in the supercontinent are 30–70 MPa	Incomplete cycle, one immobile supercontinent
6	Yoshida (2010)	Spherical model with temperature dependent viscosity in the mantle, Ra = 1 × 10^7. Supercontinent is modelled as a undeformable, immobile, highly viscous supercontinental lid	Tensional deviatoric stresses in the supercontinent are 30–90 MPa	Incomplete cycle, stage of immobile supercontinent
7	Bobrov and Baranov (2011)	2-D (1:5) models with isoviscous, four layered and p, T dependent viscosity mantle, Ra = 2 × 10^7. Continent is modelled by the active markers with increased viscosity and low density	Tensional stresses in the continent reach 4 MPa, compressive stresses in the continent can reach 35 MPa	Incomplete cycle, one mobile continent
8	Zhang et al. (2018)	Spherical model with non-Newtonian rheology, Ra = 1.5 × 10^8. Supercontinent is modelled by compositionally buoyant and highly viscous tracers with pre-existing weak continental margins	Extensional stresses in the supercontinent reach 40 MPa at the central area of the supercontinent and 15 MPa at its edge	Incomplete cycle, the breakup of supercontinent.
9	Bobrov and Baranov, (2019)	2-D (1:10) model with p, T and stress dependent viscosity, Ra = 2.5 × 10^7. Continents were modelled by the active markers with increased viscosity and low density	Before the breakup maximum shear stress generated in the supercontinent can reach 200 MPa.	Incomplete cycle, five continents, the breakup of supercontinent

(Continued on the following page)

TABLE 1 (*Continued*) Studies investigating stresses in the supercontinent.

No	Paper	Type of model	Stresses	Supercontinent cycle
10	Yoshida (2019)	Spherical model with p, T, stress dependent viscosity in the mantle, Ra = 5.89 × 10^7. Continents are modelled by a compositionally buoyant and viscous tracers	Tensional and compressional stress acting under the moving continents reach 100 MPa.	Incomplete cycle, formation of a new supercontinent
11	Huang et al. (2019)	Spherical model with non-Newtonian rheology, Ra = 8 × 10^7. Supercontinent is modelled by compositionally buoyant and highly viscous tracers with pre-existing weak continental margins and orogens	Case of homogeneous supercontinent 20–50 MPa extensional stress in its interior (<40° from the center) Supercontinent with orogens: the extensional stress focuses on the top 80-km of the continental lithosphere, the average magnitude ~160 MPa. At the margin of the supercontinent the extensional stress is about 5–50 MPa.	Incomplete cycle, the breakup of supercontinent.
12	Bobrov et al. (2022)	2-D (1:10) model with non-Newtonian rheology, Ra = 2.5 × 10^7, phase transitions, oceanic crust and deformable continents modelled by the active markers with increased viscosity and low density	Maximum tensional stress in the supercontinents can reach 200–250 MPa.	Full irregular cycle, five continents

Here, Ra is the thermal Rayleigh number; p, pressure, T, temperature.

With the definition taken here (Equations 4, 5), the compressive stresses are negative. For both, p and τ, the dimensional unit σ is $\sigma_0 = \kappa\eta_0/R^2 = 0.124 \times 10^3$ Pa. Hence, for example, the non-dimensional value of σ = 400,000 corresponds to the dimensional value of $\sigma_0 \cdot \sigma$ = 50 MPa.

The non-dimensional depth (r) and temperature-dependent viscosity are defined as follows:

$$\eta(T,z) = \eta_z \exp\left(-ET + 2.3(2.2 - 2.2r)\right), \quad (6)$$

where η_z is the depth pre-factor, and E is the activation energy of olivine.

2.2 Modeling parameters and initial conditions

Our numerical model has six parameters, specifically the thermal Rayleigh number Ra, two phase Rayleigh numbers Ra_{ph410} and Ra_{ph660}, the depth-dependent viscosity pre-factor η_z, the internal heat generation rate H, and the activation energy E = 9.2 (Equation 6) that gives rise to 10^3 viscosity variations for the temperature varying from 0 to 1 (without a supercontinent). The viscosity jump between the upper and lower mantle was set 30 in agreement with previous studies (e.g., Bunge et al., 1996; Phillips and Bunge, 2005; 2007; Zhong et al., 2007; Zhang et al., 2009). We also increased the viscosity of the oceanic lithosphere (compared to the temperature-dependent viscosity) by an additional factor of 20 in the upper layer of 70 km.

The modelled supercontinent has the shape of a spherical cap centered at the South Pole and is limited by a latitude of 66.4° (i.e., $\theta \le 66.4°$). The sub-continental lithosphere, defined as a fixed highly viscous super-continental lid (HVSL), extends down to depth of 200 km, which is consistent with recent tomography and mantle models (Becker and Boschi, 2002; Gung et al., 2003). The HVSL has a non-dimensional viscosity of 1,000, whereas the viscosity within a surrounding mantle varies from $10^{-1.5}$ to $10^{1.5}$. With such a viscosity pattern, the continent can be considered as a quasi-solid body (e.g., Trubitsyn et al., 2006). The ratio of the inner to the outer radii is 0.5448, which corresponds to the Earth's core size.

In numerical modeling, we used the CitcomS spherical code with some original improvements (Zhong et al., 1998; Tan et al., 2002; Chuvaev et al., 2020). This code has been extensively used and thoroughly tested (e.g., Schmeling et al., 2008; Zhong et al., 2008). Here the momentum transfer (Stokes) equation was solved by the finite element method (FEM) in the natural velocity-pressure variables (Hughes, 1987) by using an iterative multigrid solution method. Details on the method applied are given in Moresi and Gurnis (1996) and Zhong et al. (2000). To improve the accuracy of solution, the code uses the Uzawa's algorithm (Fortin and Fortin, 1985; Pelletier et al., 1989) which allowed us to obtain a velocity field for large viscosity variations. The parameter of artificial compressibility was assumed to be 5 × 10^{-6}, and the accuracy of the Uzawa algorithm was 1 × 10^{-6}. The heat transfer equation was solved by applying the Petrov-Galerkin method (Brooks and Hughes, 1982). The mesh is 33 × 33 × 59 × 12 cells multigrid (Zhong et al., 2000), corresponding to a vertical resolution of 50 km

TABLE 2 Parameters of a base mantle model adopted in this study.

Symbols	Meanings	Values
R	Earth's radius	6,371 km (dimensionless 1.0)
R_{core}	Radius of the Earth`s core	3,471 km (dimensionless 0.5448)
g	Gravitational acceleration	9.8 m s^{-2}
ρ_0	Reference density	4,600 kg m^{-3}
α_0	Thermal expansivity	2×10^{-5} K^{-1}
ΔT	Superadiabatic temperature difference across the mantle	2,500°
T_{top}	Temperature on the surface	0°
T_{bottom}	Superadiabatic temperature on the bottom (Core-mantle boundary)	2,500°
H	Internal heating rate	120
κ	Reference thermal diffusivity	10^{-6} m^2 s^{-1}
Ra	Rayleigh number	1.2×10^8
χ_{410}	Clapeyron slope at 410-km phase transition	1.6 MPa K^{-1}
χ_{660}	Clapeyron slope at 660-km phase transition	−1.3 MPa K^{-1}
$\Delta\rho_{410}$	Density contrast at 410-km phase transition	0.07
$\Delta\rho_{660}$	Density contrast at 660-km phase transition	0.09
Ra_{ph410}	410 km phase Rayleigh number	1.68×10^8
Ra_{ph660}	660 km phase Rayleigh number	2.16×10^8
η_0	Reference viscosity	0.5×10^{22} Pa s
η_z	depth prefactor, lithosphere (0-70 km)	20
η_z	depth prefactor, upper mantle (70-660 km)	1
η_z	depth prefactor, lower mantle (660-2900 km)	30
η_{HVSL}	$\theta \le 66.4°$ (southern hemisphere), depth 0-200 km	1,000

according to mantle tomography models (e.g., Becker and Boschi, 2002). The calculation was carried out on a personal computer with 18 GB of RAM and 8 cores (Intel Core i7) on a VmWare virtual machine by using virtualization technology (Chuvaev et al., 2020). The computation time of one model was approximately 1 month.

Firstly, we computed a pure thermal convection model until quasi steady-state solution was reached. This model started from a radial temperature profile with horizontal perturbations. After reaching a quasi-steady-state solution (temperature field), we added the supercontinent as a high viscous block and used temperature field as an initial condition to restart calculation. This method was used before, for instance, by Zhang et al. (2009), Honda et al. (2000), or Phillips and Bunge (2007).

In addition to the base model (model 1), with the parameters summarized in Table 2, three other models were calculated: the model 2 with a thin supercontinent (100 km) with the same parameters as in model 1, the model 3, including a weak zone around the supercontinent, and the model 4, with the Rayleigh number halved ($R = 6 \times 10^7$) and with the internal heat production number halved (H = 60).

3 Results

The results of numerical modeling make it possible to identify some specific features for the fields that arise under the influence of the supercontinent. At first, the pure thermal convection model

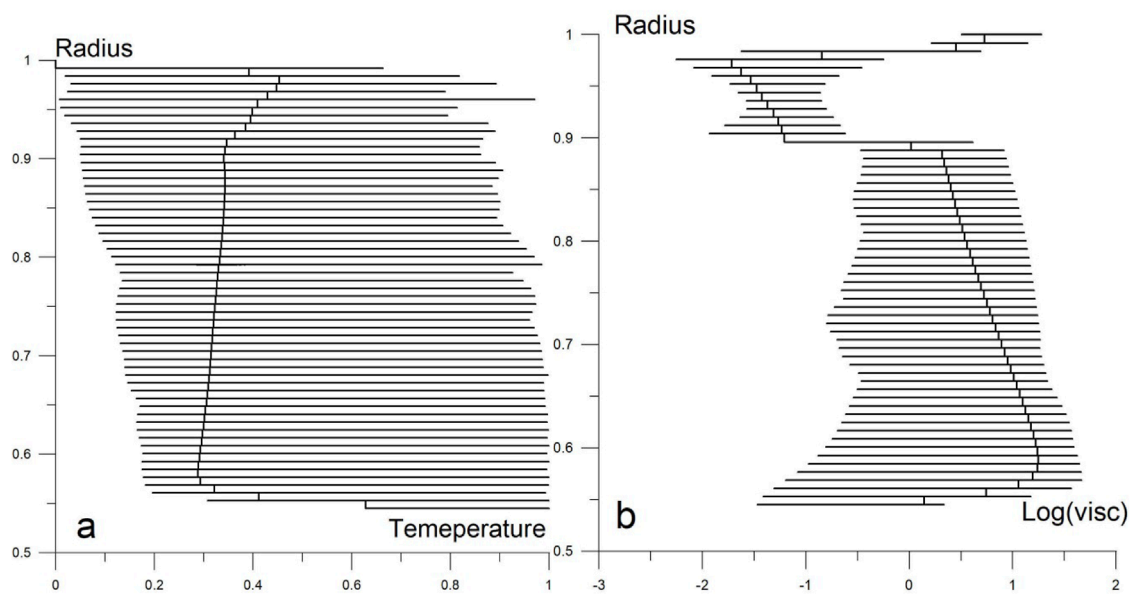

FIGURE 1
The mantle model for quasi-steady state without supercontinent. The depth distribution of dimensionless superadiabatic temperature **(a)** and viscosity **(b)** respectively.

reaches the regime when the systematic trend of the solution disappears (Figure 1). Figure 1 shows the distribution of the average superadiabatic temperature (Figure 1a) and the logarithmic viscosity (Figure 1b) for the entire mantle. After that, we introduced the supercontinent as a highly viscous super-continental lid. Then we calculated the mantle convection over the period of ~160 Ma. The mantle flow, temperature, viscosity, and the distribution of lateral stresses $\sigma_{\theta\theta}$ for different time stages and sections are presented on Figures 2–9 (base model). Figures 2, 4, 6 show calculated fields of the dimensionless temperature, the logarithmic viscosity, and the lateral stresses $\sigma_{\theta\theta}$ in the spherical section along the longitude of $\phi = 20°$ and 200° at three successive stages (0, 80, and 160 Ma). Figures 3, 5, 7 show the calculated fields of temperature and lateral stresses for the same epoch times at depths of 100 and 300 km in the Mollweide (Babinet) projection.

The viscosity field exhibits the presence of a supercontinent (purple surface, lower part of Figure 2b), a jump at the 660-km phase boundary as well as the temperature-dependent nature of viscosity, and the increase of viscosity with depth. The presence of phase transition at depth of 660 km with real parameters (Table 2) does not cause separation of a mantle flows between the upper and lower mantle. As a result, at the phase boundary between the lower and upper mantle only slowing down of mantle flows is detected.

Due to a viscosity jump by a factor of 30 in the lower mantle, as well as due to an endothermic phase transition at a depth of 660–670 km, mantle flows are largely forced out into the upper mantle (Figures 2, 4, 6). The centers of convective mantle cells turn out to be elevated towards the surface, as it can be seen from the velocity vectors of mantle flows. As a result, extended regions of sub-horizontal relatively fast currents appear in the upper mantle. Similar features in the convection pattern appeared with the introduction of a phase boundary at a depth of 660 km in the isoviscous (e.g., Bunge et al., 1996) and temperature-dependent viscosity models (e.g., Zhong et al., 2000).

3.1 Evolution of temperature and mantle flows

After the supercontinent implementation, the thermal-blanket effect of the supercontinent begins to influence on the mantle convection pattern. Due to a high viscosity, the velocities in the supercontinent become small and convective transport in the supercontinent stops. Only conductive heat transfer in the supercontinent takes place. As a result, the supercontinent becomes a region of low temperatures compared to the convecting mantle at the same depth, as seen in Figures 5a, 7a for the depth of 100 km. At the lower boundary of the continental lithosphere at a depth of 200 km, temperatures in the subcontinental mantle and in the continental lithosphere become equal. Below the supercontinent, positive temperature anomalies are formed due to a thermal insulation. Our numerical modeling revealed that over time, hot mantle upwellings tend to concentrate under the supercontinent, as seen in Figures 5c, 7c for the depth of 300 km. In addition, their upper part increases because it cannot effectively shed heat through a lower boundary of the supercontinent. As a result, the average temperature in the area under the supercontinent rises over time and becomes higher than the average temperature of the sub-oceanic area, where cold descending mantle currents intensify. Thus, at the depth of 100 km, the temperature in the supercontinent is lower by an average of 250 K (compared to the surrounding mantle) (see Figure 7a), while at the depth from 300 to 400 km under the

10.3389/feart.2025.1452399

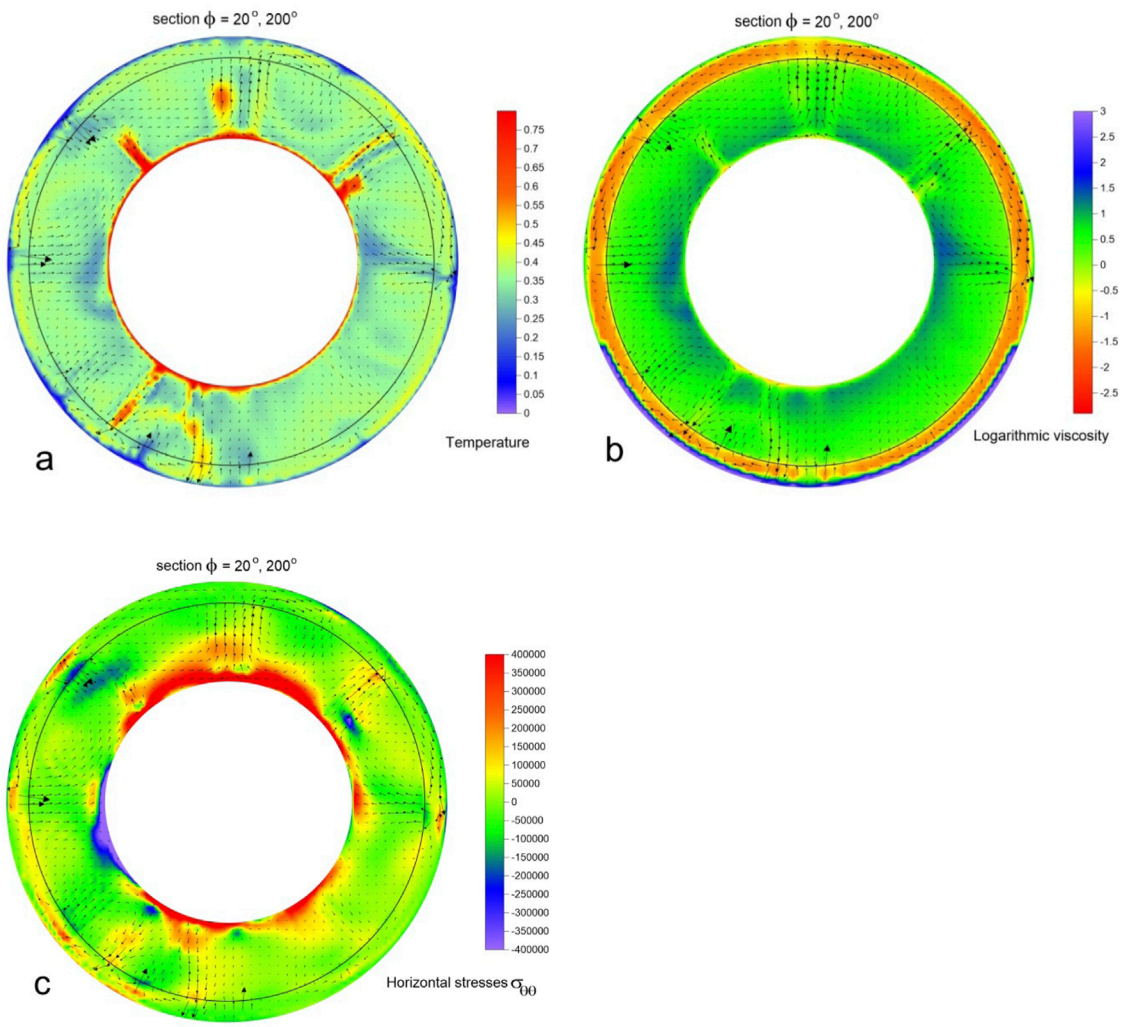

FIGURE 2
The base mantle model, the moment of supercontinent (200 km thickness) implementation, stage t = 0 Ma. The black ring shows the boundary of the upper mantle at a depth of 660 km. From top to bottom: **(a)** section φ = 20° and 200° of the spatial distribution of the dimensionless temperature, the flow velocities are shown by the black arrows; **(b)** section φ = 20° and 200° of the spatial distribution of the dimensionless logarithm viscosity with flow velocities; and **(c)** section φ = 20° and 200° of the field of the dimensionless normal horizontal stress $\sigma_{\theta\theta}$ with flow velocities.

supercontinent, the temperature of the subcontinental mantle is higher on average by 60 K (Figure 7c).

The phenomenon of a partial concentration of mantle upwellings under the supercontinent is already clearly manifested at t = 80 Ma after the supercontinent implementation (Figure 5c), while in the oceanic region opposite to the supercontinent, descending mantle flows are more pronounced. However, mantle upwellings continue to exist in the oceanic region, participating near the surface in the formation of convection cell structures surrounded by subduction zones (Figures 5a, 7a). Further, this feature of a mantle convection pattern is preserved (Figure 7c). Annular sections of the mantle show similar features of the temperature distribution over depth in sections of φ = 20° and 200° (Figures 4a, 6a). A subduction girdle is also formed around the supercontinent. The extent of such subduction zones is approximately more than half of its continental-oceanic boundary, e.g., (Figures 5a, 7a).

3.2 Evolution of the stress field $\sigma_{\theta\theta}$

After the implementation of a supercontinent, the $\sigma_{\theta\theta}$ stresses in the mantle areas where there are no strong current velocity gradients (the main part of the mantle) are in the range of about ±120,000 in non-dimensional form (±15 MPa in dimensional form).

Downwelling/upwelling mantle flows differ in the $\sigma_{\theta\theta}$ stress field from the surrounding mantle regions by approximately ±200,000 (±25 MPa). These areas are clearly visible in Figures 3b–d. The strongest stresses are detected in the lowermost mantle. This might be explained by a vertical temperature gradient being stronger than at the outer surface due to the difference in the areas of these surfaces in the considered spherical problem.

After the implementation of a supercontinent in our model, stress fields in the spherical segment of supercontinent begin to change. The concentration of hot mantle flows under the supercontinent that forms as described above, significantly changes

10.3389/feart.2025.1452399

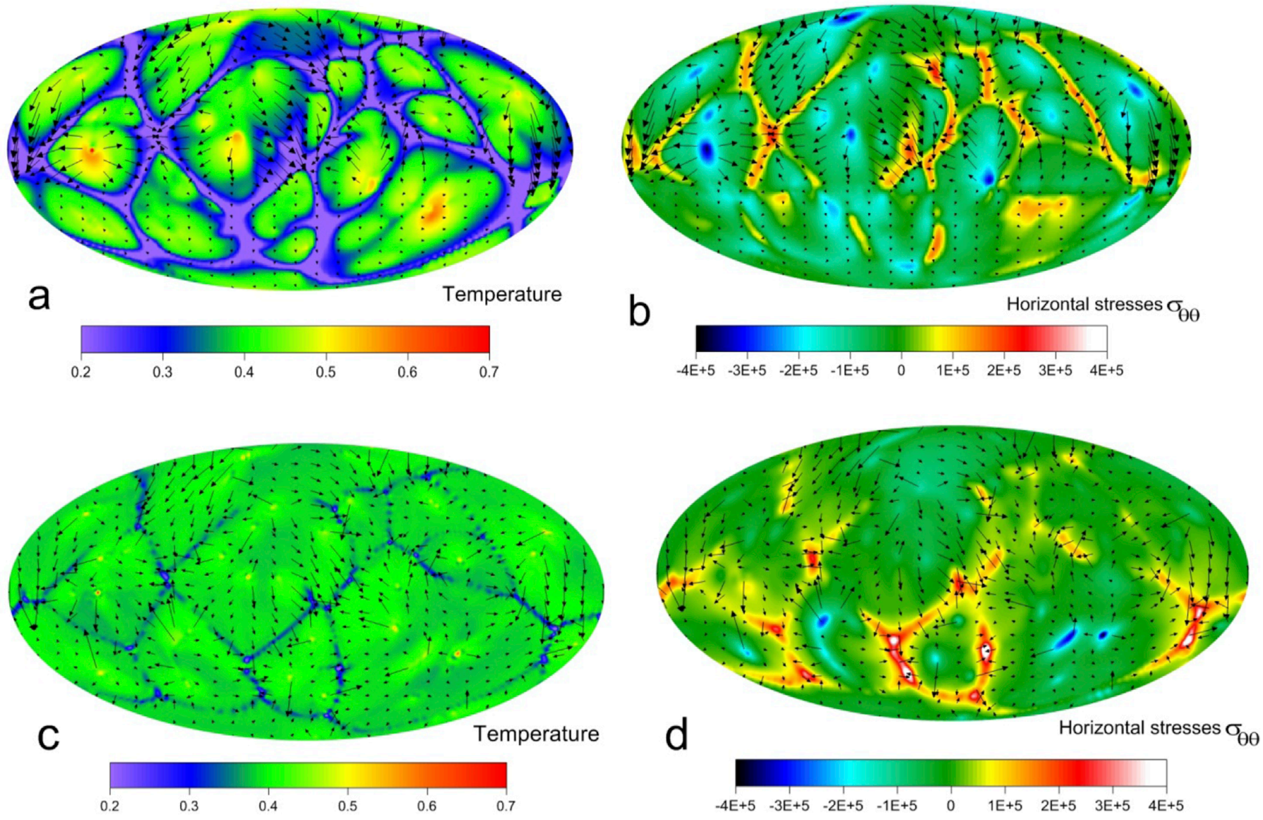

FIGURE 3
The base mantle model, the stage t = 0 Ma in the Mollweide (Babinet) projection. From top to bottom: **(a)** section on depth of 100 km, the spatial distribution of the dimensionless temperature, the flow velocities are shown by the black arrows; **(b)** section on depth of 100 km, the field of the dimensionless normal horizontal stress $\sigma_{\theta\theta}$; **(c)** section on depth of 300 km, the spatial distribution of the dimensionless temperature, the flow velocities are shown by the black arrows; and **(d)** section on depth of 300 km, the field of the dimensionless normal horizontal stress $\sigma_{\theta\theta}$.

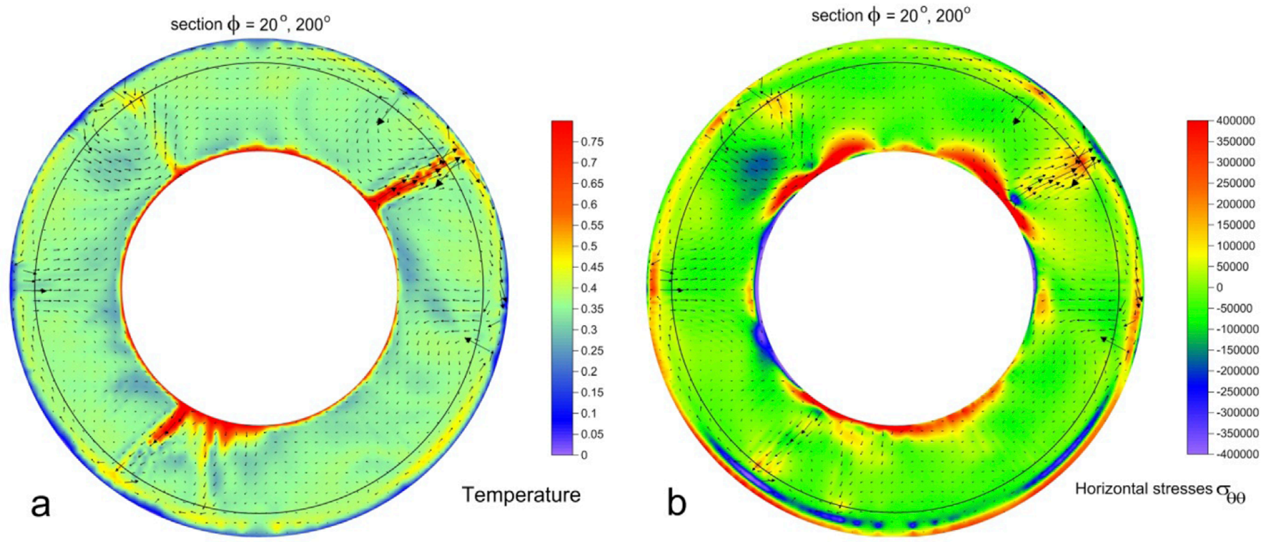

FIGURE 4
The base mantle model, the continent thickness is 200 km, and the stage t = 80 Ma. The black ring shows the boundary of the upper mantle at a depth of 660 km. From top to bottom: **(a)** section φ = 20° and 200° the spatial distribution of the dimensionless temperature, the flow velocities are shown by the black arrows; and **(b)** section φ = 20° and 200° the field of the dimensionless normal horizontal stress $\sigma_{\theta\theta}$ with flow velocities.

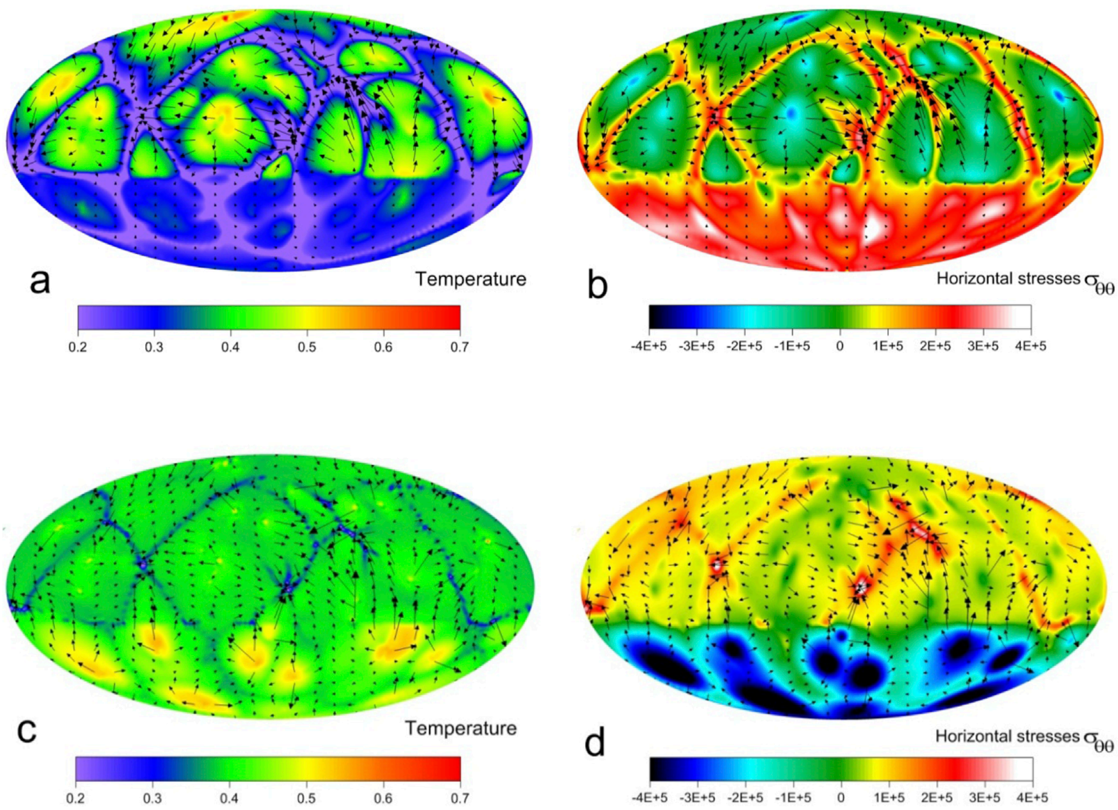

FIGURE 5
The base mantle model, the continent thickness is 200 km, and the stage t = 80 Ma. See Figure 3 for the legend. From top to bottom: **(a)** section on depth of 100 km, the spatial distribution of the dimensionless temperature, the flow velocities are shown by the black arrows; **(b)** section on depth of 100 km, the field of the dimensionless normal horizontal stress $\sigma_{\theta\theta}$; **(c)** section on depth of 300 km, the spatial distribution of the dimensionless temperature, the flow velocities are shown by the black arrows; and **(d)** section on depth of 300 km, the field of the dimensionless normal horizontal stress $\sigma_{\theta\theta}$.

the stress pattern under and within the supercontinent. The horizontal tensional (over-lithostatic) stresses $\sigma_{\theta\theta}$ are formed in the supercontinental area (t = 80 Ma, Figure 5b). Later, the supercontinental area becomes outlined in the horizontal tensional stress field $\sigma_{\theta\theta}$ more clearly (t = 160 Ma, Figure 7b). The supercontinent is characterized by horizontal over-lithostatic tensional stresses $\sigma_{\theta\theta}$ in the range from 200,000 to 400,000 (from 25 to 50 MPa, stages t = 80 Ma, Figure 5b; t = 160 Ma; Figure 7b, red and orange colors). In contrary, after the rearranging of mantle flows under the supercontinent, these mantle upwellings produce horizontal over-lithostatic compressive stresses $\sigma_{\theta\theta}$ in the range from 160,000 to 480,000 (from 20 to 60 MPa, stages t = 80 Ma, Figure 5d; stages t = 160 Ma; Figure 7d, blue colors).

As the results of the $\sigma_{\theta\theta}$ fields show, the location of the heads of ascending mantle flows under the supercontinent is quite clearly exhibited. In the lithosphere of the supercontinent, this location is also pronounced, but somewhat less; rather, there is general stretching of the supercontinent, with some variations across its regions.

We also traced changes in the $\sigma_{\theta\theta}$ field depending on depth, for depths of 500, 1,500, and 2,550 km (Figures 8a–c). The result shows that at depth of 500 km, the difference between the sub-supercontinental region (which is generally in a state of compression, blue tones) and the suboceanic region is pronounced, but significantly less than at depth of 300 km, as discussed earlier. At depth of 1,500 km, the difference between the sub-supercontinental and suboceanic regions is manifested in the fact that all downwelling flows are located in the suboceanic region. At this depth, lateral linear structures tend to disappear, and the most intense mantle flows are subvertical and have relatively small diameter. Accordingly, the stress fields also change. As seen in Figure 8b, the stress values almost everywhere at depths of 500 and 1,500 km are much smaller than in the mantle boundary layers. Moreover, stresses also drop in submerging linear structures. At depth of 2,550 km, when the currents interact with the lower boundary of the mantle, the stresses increase substantially (Figure 8c). The appearance of quasi-linear structures is again observed, however, now these are not cold descending, but hot ascending mantle flows. At this depth, both in the temperature field and in the stress field, the influence of the supercontinent is not obvious.

Figure 9 shows the vertical distribution of the dimensionless temperature averaged laterally (that is, at a fixed value of the radius) over the entire computational area (black line), the stage t = 160 Ma after the supercontinent implementation. The horizontal bars display the temperature deviation range in the nodes from the mean value. A similar averaged temperature curve is also shown for

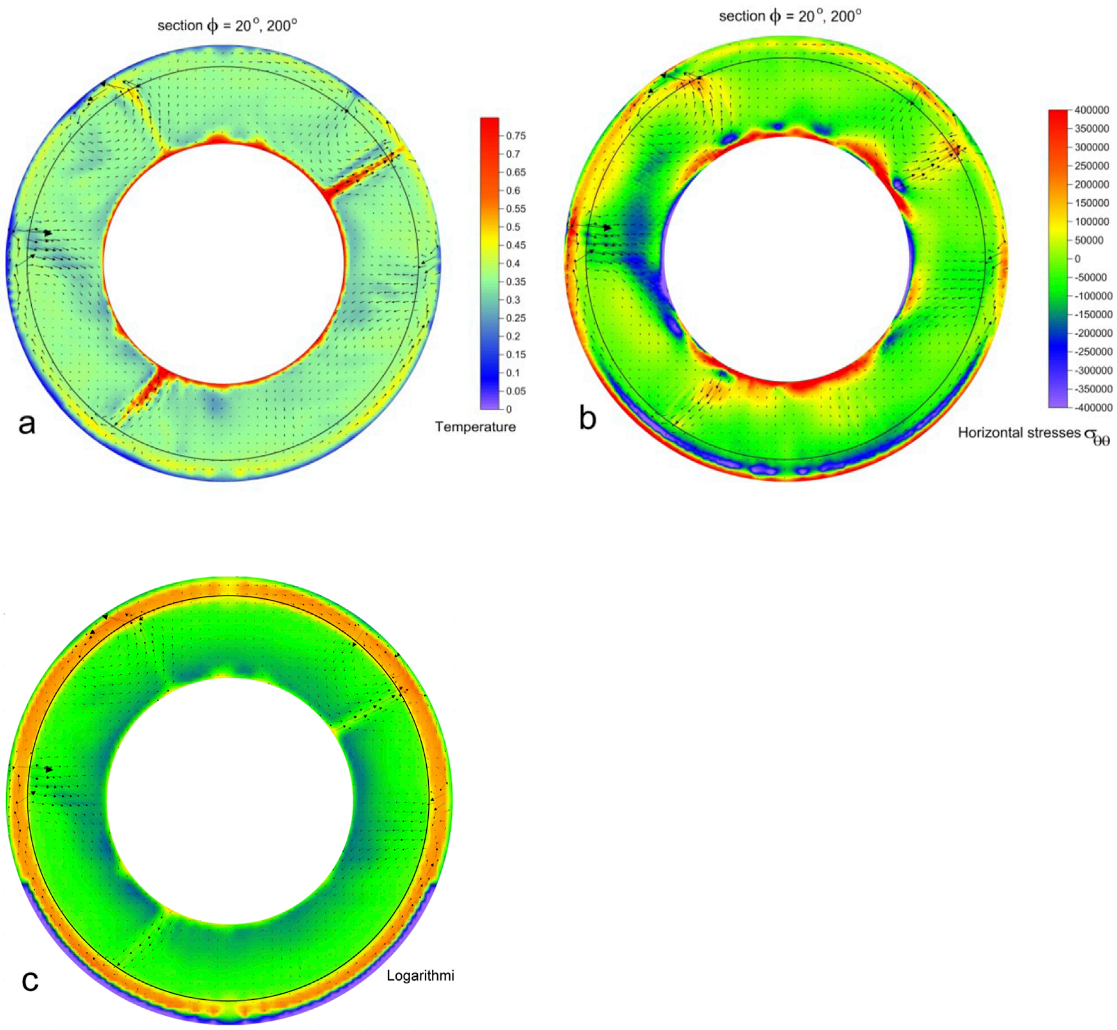

FIGURE 6
The base mantle model, the continent thickness is 200 km, and the stage t = 160 Ma. From top to bottom: **(a)** section φ = 20° and 200° the spatial distribution of the dimensionless temperature, the flow velocities are shown by the black arrows; **(b)** section φ = 20° and 200° the field of the dimensionless normal horizontal stress $\sigma_{\theta\theta}$ with flow velocities and **(c)** Section φ = 20° and 200° of the spatial distribution of the dimensionless logarithm viscosity with flow velocities.

the subcontinental area only (red line). The temperature increase below a supercontinent is clearly seen within the upper mantle. The temperature difference, however, also takes place (to a lesser extent) throughout the lower mantle, as well as in the boundary layers. In the lower boundary layer, the differences in average temperatures are pronounced. Under the supercontinent, the temperature increases up to 120 K. Thus, the effect of supercontinent is pronounced also near the lower boundary of the lower mantle. We conclude that the reason for this is the concentration of roots of ascending plumes under the continental region.

We also calculated other numerical models, for testing and comparison purposes for the same time steps. For the second model, we halved the thickness of the supercontinent to 100 km with the same other parameters. In this case extensional stresses in the supercontinent at a depth of 50 km may be 20–50 MPa whereas under the supercontinent overlithostatic compressive horizontal stresses are less than 50 MPa (Figure 10).

Another model (model 3) was considered with a weak zone of viscosity reduced by a factor of 100 along the border of the supercontinent with the same other parameters as in the base model. For this model with a weak zone, a supercontinent becomes mainly surrounded by subduction zones, while in our basic model the subduction covered only about half of the perimeter. Calculations show a trend towards an increase in tensile stresses in the supercontinent up to 100 MPa due to an increase in the extent of subduction zones at its edges (Figure 11). As in previous models, we find the concentration of hot mantle flows under the supercontinent.

Additionally, we consider model 4 with Ra = 6 × 10^7 and H = 60 without a weak zone and 200 km thickness of the supercontinent which mainly provides the same quality features of stress fields and mantle flows pattern as a base model (model 1). However, here the stress values are approximately two times smaller than in the base model.

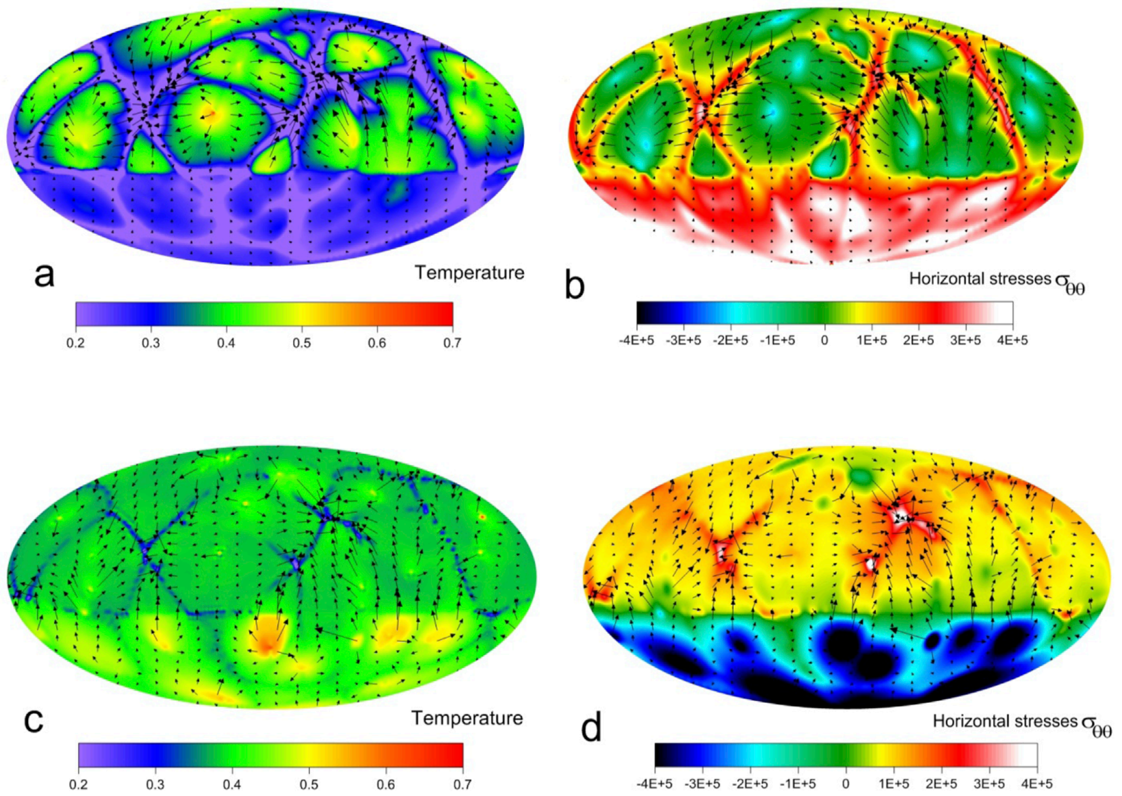

FIGURE 7
The base mantle model, the continent thickness is 200 km, and the stage t = 160 Ma. See Figure 3 for the legend. **(a)** Section on depth of 100 km, the spatial distribution of the dimensionless temperature, the flow velocities are shown by the black arrows; **(b)** section on depth of 100 km, the field of the dimensionless normal horizontal stress $\sigma_{\theta\theta}$; **(c)** section on depth of 300 km, the spatial distribution of the dimensionless temperature, the flow velocities are shown by the black arrows; and **(d)** section on depth of 300 km, the field of the dimensionless normal horizontal stress $\sigma_{\theta\theta}$.

4 Discussion

In this study we modelled the supercontinent as an immobile highly viscous lid without its breakup. Such approximation was made before, for example, by Yoshida et al. (1999) and Yoshida (2010). As shown by numerical calculations for spherical and Cartesian models (e.g., Yoshida, 2019; Bobrov et al., 2022) the velocities of a supercontinent after its formation and before its breakup are relatively small. Thus, an immobile supercontinent gives a fairly acceptable approximation for this stage of the supercontinent cycle.

We demonstrated that after implementing the supercontinent in the model, the mantle flows reorganize and a group of mantle upwellings under the supercontinent is formed whereas subduction under the supercontinent stops. Also, subduction zones (so-called subduction girdle) are formed around the supercontinent. Presence of a subduction girdle around the supercontinents has been verified for reconstructed Pangea (e.g., Collins, 2003), Rodinia (e.g., Li et al., 2008), and partly for Nuna (e.g., Pisarevsky et al., 2014).

In addition, the models exhibited a partial cooling of the supercontinent area. The temperature at the depth of 100 km in the continental lithosphere is lower by approximately 250 K compared to the surrounding mantle. The heat-insulating effect of the supercontinent leads to the concentration of mantle upwellings and an increase in temperature under a supercontinent. This leads to a slight rise in temperature within the subcontinental mantle. For example, at the depth of 300 km, positive temperature anomalies in the vast mantle area below a supercontinent range to 60–70 K (Figures 5c, 7c). The effect of thermal insulation was described in detail by Lowman and Gable (1999), Yoshida et al. (1999), Li and Zhong (2009), Heron and Lowman (2011), Yoshida (2013), Mao et al. (2019), and others (Table 1). For example, Yoshida (2013) and Heron and Lowman (2011) have calculated that a temperature increase under the supercontinent is about only 50 K. Our results show (*cf.* Figures 2a,b; Figures 4a,b; Figures 6a,b) that hot temperature anomalies are concentrated in the narrow jets while the stress anomalies are more diffuse and cover substantially larger areas. The reason is the viscous involvement of the surrounding mantle material into the upwellings. Thus, hot mantle upwellings (despite their reduced viscosity and, consequently, reduced coupling with surrounding mantle material) are nevertheless able to induce the mantle flows and the stresses in significant surrounding areas.

We also studied stress fields at large depths in the mantle and their response to the presence of a supercontinent. The effect of the implemented supercontinent on stress fields decreases with depth for all our models. At the core, the stress field is determined by the inhomogeneous structure of the mantle flows at the bottom of the mantle.

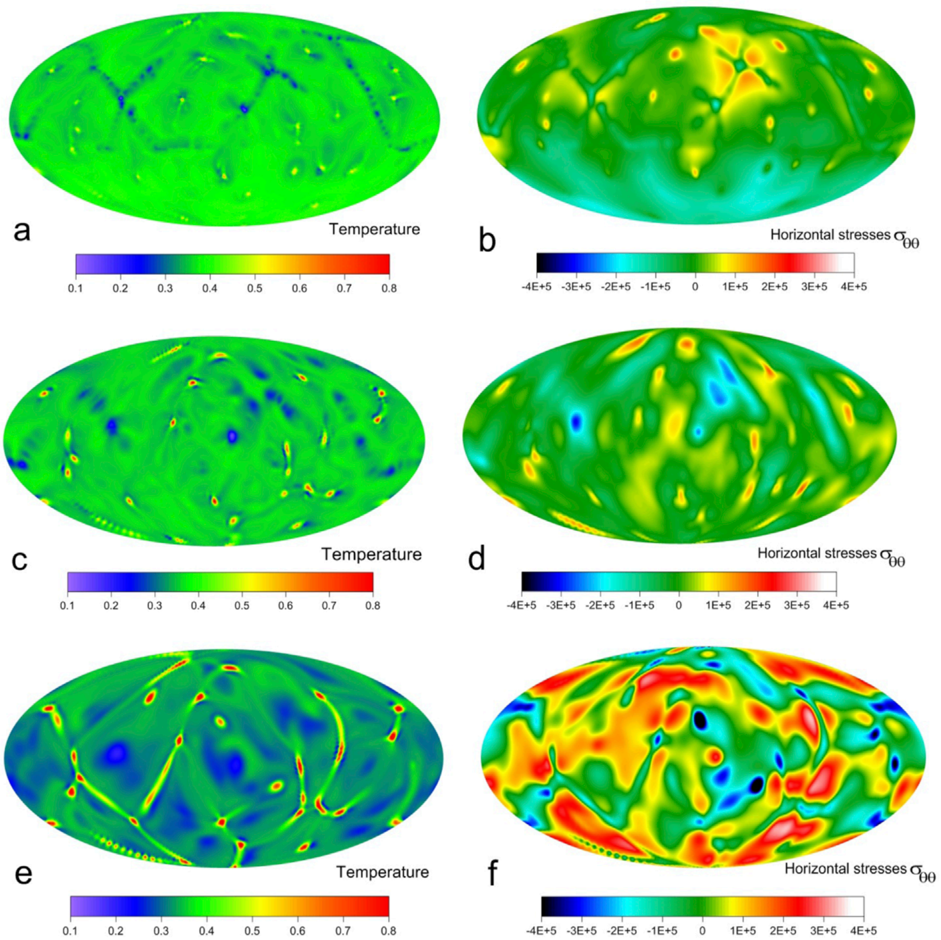

FIGURE 8
The base mantle model, the continent thickness is 200 km, and the stage t = 160 Ma. **(a)** Section on depth of 500 km, the field of the dimensionless temperature; **(b)** section on depth of 500 km, the field of the dimensionless normal horizontal stress $\sigma_{\theta\theta}$; **(c)** section on depth of 1,500 km, the field of the dimensionless temperature; **(d)** section at depth of 1,500 km, the field of the dimensionless normal horizontal stress $\sigma_{\theta\theta}$; **(e)** section on depth of 2,550 km, the field of the dimensionless temperature; **(f)** section at depth of 2,550 km, the field of the dimensionless normal horizontal stress $\sigma_{\theta\theta}$.

In addition to the main model, we investigated other scenarios. In the second model the thickness of supercontinent was reduced to a half (100 km), whereas other parameters were kept the same (Figure 10). It could be assumed that for the case of a thinner supercontinent plate, the forces acting in it per unit cross section (i.e., stresses) would be large. The results showed, however, that simultaneously, the integral tensile forces themselves, acting at the base of supercontinent, changed (decreased) as a result of the diminution of the difference between the sub-supercontinental and the suboceanic region. As a result, the influence of the supercontinent thickness on tensile stresses turned out to be insignificant; the difference was rather in a more non-uniform distribution of stresses in the supercontinent compared to a main model. Thus, both models demonstrate the maximum value of $\sigma_{\theta\theta}$ around 50 MPa, which is consistent with the results of Huang et al. (2019) for the case of the absence of a weak zone along the perimeter of the supercontinent.

Another model (model 3) with a weak zone around the supercontinent provides the subduction girdle around the supercontinent (Figure 11). Similar to the results obtained in the other studies (e.g., Huang et al., 2019), the model showed the emergence of a robust annular subduction zone around the supercontinent, while in our basic model the subduction covered about half of the perimeter. The presence of this extensive circumferential subduction leads to an increase in tensile stresses in the supercontinent. Here extensional stresses in the supercontinent reach 100 MPa. Since the compressive stresses below the supercontinent are also increased, we conclude that this phenomenon is related to increased volume of downwelling hence increased upwelling leading to higher stresses.

We also considered the model 4 with halving the Rayleigh number and with halving the heat generation from our base model 1. Here, the stresses in and under the supercontinent turn out to be about half as much as for our basic model, which is not enough for the breakup of the supercontinent. We, therefore, concluded that the real values of Rayleigh number and heat-flow generation should be higher than in this model.

Unlike previous studies, we also investigated the stress fields in the meridional annular section of the mantle, which makes

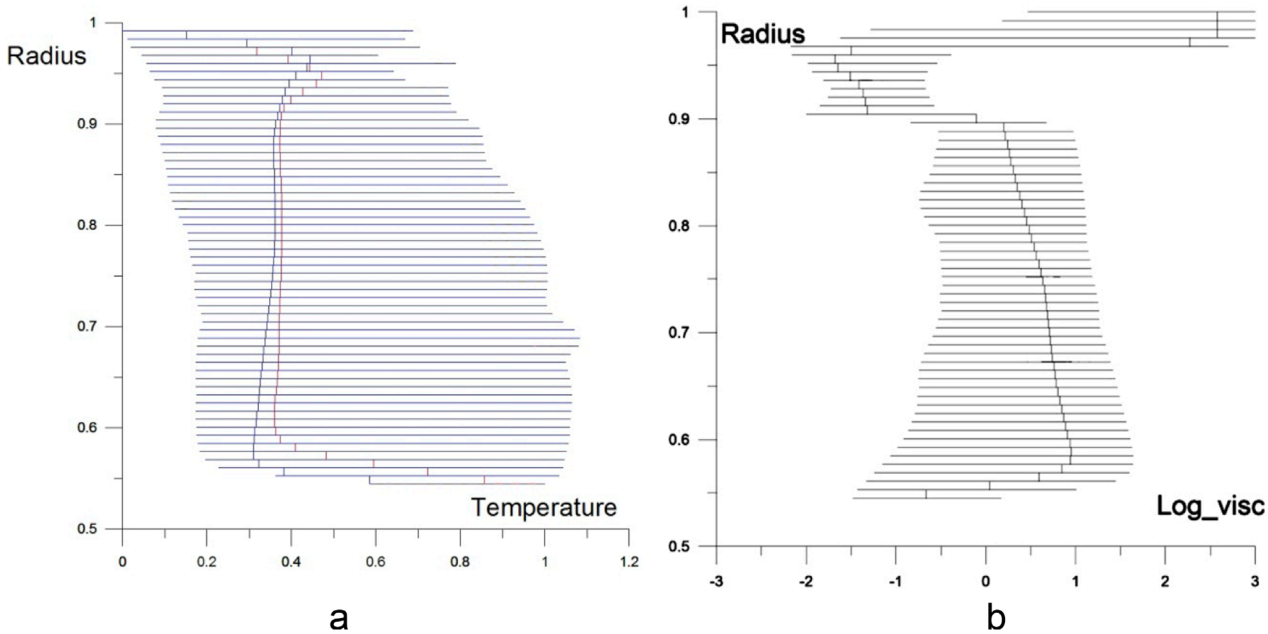

FIGURE 9
The mantle model, the stage t = 160 Ma. The laterally averaged depth distribution of dimensionless temperature **(a)** and viscosity **(b)** respectively. The red line shows the average temperature curve for the subcontinental area only. The blue line shows the average temperature curve for the entire mantle.

it possible to analyze the stresses at all its depths. Calculated horizontal stresses ($\sigma_{\theta\theta}$) revealed sharp change in the sign of $\sigma_{\theta\theta}$ with depth at the transition from the supercontinent to the underlying mantle (e.g., sharp change of red to blue colors in the lower part of Figure 6b). Well defined horizontal tensional over-lithostatic stresses (red and orange colors in Figures 5b, 7b) developed in the supercontinent above mantle upwellings. The figures of meridional annular sections e.g., Figure 6b show some blurring of the change in the sign of $\sigma_{\theta\theta}$ with depth. Nevertheless, we state that according to the calculation results, the lowest calculation nodes, lying in the supercontinent, almost all show tensile stresses while the next row of grid nodes, lying already in the subcontinental mantle, almost everywhere show compression stresses.

At the stage of t = 160 Ma (see Figure 7b), they reached up to 400,000 dimensionless units (50 MPa in dimensional form). These values closely agree with the results presented by Zhang et al. (2018) for depths of 75 km and 220 km. This relatively low value may also be caused by the spherical effect (e.g., Butler and Jarvis, 2004). It may not be sufficient for a supercontinent breakup. However, for the model 3 with a weak zone around the supercontinent the tensional stresses are more reliable (Figure 11). In contrary, in vast areas of the subcontinental mantle corresponding to the heads of mantle upwellings, we find a pronounced horizontal compressive stress (blue and purple colors in Figures 5d, 7d). For example, in Figure 7d in the subcontinental mantle the overlithostatic compressive stresses range from 200,000 to 400,000 in the dimensionless form (from 25 MPa to 50 MPa). The boundary of a sharp change in the values of $\sigma_{\theta\theta}$, which appears in these areas, outlines the position of effective viscosity jump, meaning that this interface marks the base of the HVSL.

The reason for this difference in stresses in the supercontinent and the underlying mantle is the strong difference in viscosities of the continent and the underlying mantle material. The supercontinent material, due to its high viscosity, cannot move in the same way as the underlying mantle. This effect in the area under the supercontinent is clearly visible in Figures 5b,d as well as in Figures 7b,d.

It is important to note that the same phenomenon of a sharp contrast and reversal of $\sigma_{\theta\theta}$ stress sign is also presented in oceanic areas on the lithosphere-asthenosphere boundary. For example, in Figure 6b, an upwelling mantle flow (in the upper left of the figure) creates tensile stresses in a relatively thin oceanic lithosphere and compressive stresses immediately below it. In contrast, the descending mantle flow (left side of the same figure, equatorial region) creates compressive stresses in the oceanic lithosphere and tensile stresses immediately below it. The over-lithostatic tensile stresses arise in a relatively thin oceanic lithosphere above the layer with upward-moving flows where the horizontal stresses are compressive (Figure 6b, left side). Our results revealed that the difference in viscosities of two orders is already sufficient for the appearance of this phenomenon.

Our model cannot provide the plate behavior due to small laterally viscosity variations. By this reason slabs and mantle plumes in our model are absent. However our results are in a good agreement with other spherical models where stresses were studied (e.g., Huang et al., 2019; Yoshida, 2019; 2010). Numerical modeling was performed with a realistic Rayleigh number, phase transitions and p, T dependent viscosity. Despite a rather rough resolution grid, it was enough to resolve small-scale mantle plumes under the supercontinent. Used rheology generates the long-wavelength

10.3389/feart.2025.1452399

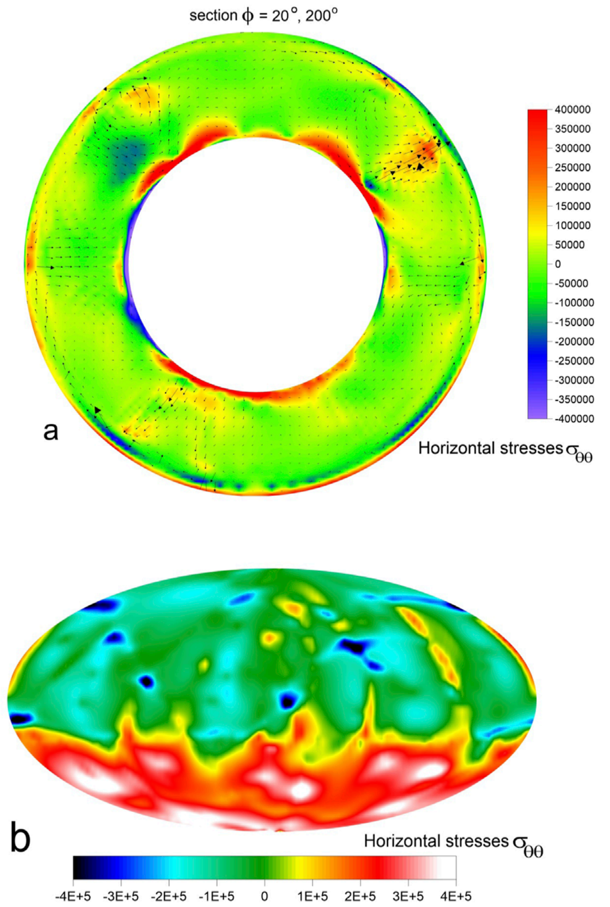

FIGURE 10
The second mantle model, the continent thickness is 100 km, and the stage t = 160 Ma. **(a)** Section φ = 20° and 200° the field of the dimensionless normal horizontal stress $\sigma_{\theta\theta}$ with flow velocities. The black ring shows the boundary of the upper mantle at a depth of 660 km. **(b)** The field of the dimensionless normal horizontal stress $\sigma_{\theta\theta}$ (depth 50 km).

convective structures; however, it is not able to produce strong plates for oceanic regions.

Compared to other studies we focused on stresses not only in the supercontinent. For example, Yoshida (2010) considered stresses at the depths of 43, 129 and 215 km, that is, in the supercontinent and at its base. Huang et al. (2019) considered stresses only for depths of 220 km, and in the form of one-dimensional profiles averaged over both angular coordinates (not in the form of a map). We argue that it is essential to study the stresses not only within the supercontinent, but essentially throughout the whole mantle down to the core-mantle boundary in order to better understand supercontinent cycle. Moreover, the analysis of only averaged values does not provide the whole picture. Instead, the analysis should involve also the ranges of their lateral variations and the peculiarities of separate typical regions (upper mantle, lower mantle, its lowermost part, areas of the ascending and descending mantle flows).

Unlike mantle models from Huang et al. (2019) and Zhang et al. (2018) who considered a supercontinent breakup, our models do not incorporate continental breakup process yet. This requires adding active tracers that will be implemented in our forthcoming study. It is also important to note that some other essential factors, such as plates-like behavior, should be incorporated into the model. However, in contrast to these studies, we considered and analyzed the stress fields throughout the mantle, and not only at shallow depths.

The compressive stresses in the subcontinental mantle with a strongly tensional stress directly in the supercontinent were previously shown for 2-D Cartesian mantle models with floating continents by Bobrov et al. (2022). It should also be noted that for a 2-D model with non-Newtonian stress-dependent rheology (Bobrov et al., 2022), the maximum stress values in the supercontinent (about 200 MPa) were higher than in the underlying mantle (50–100 MPa), while in our models (model 1, 2, 4), the compressive stresses under supercontinent are approximately the same by absolute value as tensional stresses in the supercontinent (values in the interval from 25 to 50 MPa).

5 Summary and concluding remarks

Using the spherical mantle convection model with the pressure- and temperature-dependent rheology, we computed the normal horizontal stresses $\sigma_{\theta\theta}$ and their temporal changes within the supercontinent and the underlying mantle. For the spherical mantle models, a successive concentration of head parts of upwellings under the supercontinent and their increasing in size, together with the intensification of slabs in the oceanic hemisphere, was shown. At the same time, the average temperature under the supercontinent rises on average by 60 K, whereas under the base of the lithosphere increase in temperature can reach up to 120 K. In the D`` layer temperature under the supercontinent is also increased up to 120 K due to mantle upwellings roots.

After the implementation of the immobile supercontinent, the area of supercontinent is limited by a spherical angle ($\theta \leq 66.4°$) of the spherical polar grid, change of the sign in horizontal stresses when moving from the region of the supercontinent to the underlying mantle is formed. The same effect is shown for the oceanic lithosphere on the lithosphere-asthenosphere boundary. Our calculations show that the overlithostatic horizontal stresses in the upper mantle are in the range of about ±15 MPa, while along the ascending and descending mantle flows these stresses are about ±25 MPa and more. The lowermost part of the lower mantle as an area of high viscosity in the presence of a significant vertical temperature gradient, exhibits the maximum stresses (up to 70 MPa).

In the supercontinent, the horizontal stresses are more moderate. For a given p, T dependent rheology in our models, the tensile stresses reach a maximum value of about 20–50 MPa. Only for model with weak zone around the supercontinent tensile stresses can reach 100 MPa due to powerful subduction girdle at its edges. A tensional regime prevailing in the supercontinent may provide the penetration of mantle upwellings into the supercontinent, followed by a decrease in the strength of this area and the supercontinent breakup. In the subcontinent mantle the overlithostatic compressive horizontal stresses are the same in the absolute value (25–50 MPa)

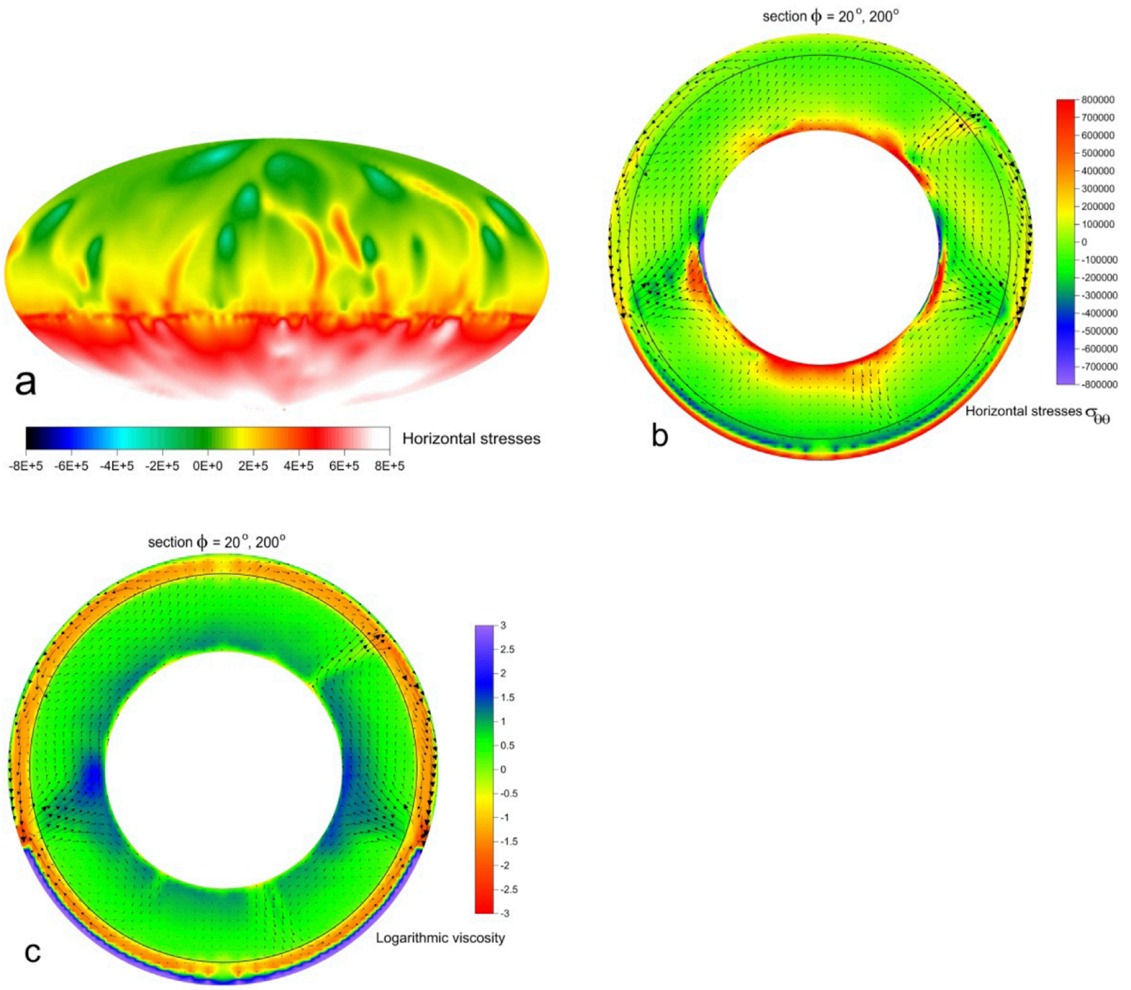

FIGURE 11
The third mantle model, the continent thickness is 200 km, and the stage t = 160 Ma. **(a)** The field of the dimensionless normal horizontal stress $\sigma_{\theta\theta}$ (depth 100 km). **(b)** Section φ = 20° and 200°, the field of the dimensionless normal horizontal stress $\sigma_{\theta\theta}$ with flow velocities. **(c)** Section φ = 20° and 200° of the spatial distribution of the dimensionless logarithm viscosity with flow velocities. The black ring shows the boundary of the upper mantle at a depth of 660 km.

except the model with weak zone where stresses are approximately twice higher.

Data availability statement

The raw data supporting the conclusions of this article will be made available by the authors, without undue reservation.

Author contributions

ABa: Investigation, Writing – original draft, Writing – review and editing. ABo: Conceptualization, Formal Analysis, Investigation, Writing – original draft, Writing – review and editing. RT: Funding acquisition, Investigation, Methodology, Project administration, Resources, Supervision, Writing – original draft, Writing – review and editing. AC: Conceptualization, Software, Writing – review and editing.

Funding

The author(s) declare that financial support was received for the research and/or publication of this article. Robert Tenzer was supported by the project P0054667 of the Land Surveying and Geo-Informatics, Hong Kong Polytechnic University.

Acknowledgments

The authors would like to thank the reviewers, whose reviews helped to improve the manuscript significantly. We are grateful to Louis Moresi, Shijie Zhong, Michael Gurnis, and other authors of the CitcomS code for providing the possibility of using this software.

Conflict of interest

The authors declare that the research was conducted in the absence of any commercial or financial relationships that could be construed as a potential conflict of interest.

Publisher's note

All claims expressed in this article are solely those of the authors and do not necessarily represent those of their affiliated organizations, or those of the publisher, the editors and the reviewers. Any product that may be evaluated in this article, or claim that may be made by its manufacturer, is not guaranteed or endorsed by the publisher.

References

Anderson, D. L. (1982). Hotspots, polar wander, Mesozoic convection and the geoid. *Nature* 297, 391–393. doi:10.1038/297391a0

Becker, T. W., and Boschi, L. (2002). A comparison of tomographic and geodynamic mantle models. *Geochem. Geophys. Geosyst.* 3. doi:10.1029/2001gc000168

Bobrov, A., Baranov, A., and Tenzer, R. (2022). Evolution of stress fields during the supercontinent cycle. *Geodesy Geodyn.* 13, 363–375. doi:10.1016/j.geog.2022.01.004

Bobrov, A. M., and Baranov, A. A. (2011). Horizontal stresses in the mantle and in the moving continent for the model of two-dimensional convection with varying viscosity. *Izv. Phys. Solid Earth.* 47 (9), 801–815. doi:10.1134/S1069351311090023

Bobrov, A. M., and Baranov, A. A. (2014). The structure of mantle flows and stress fields in a two-dimensional convection model with non-Newtonian viscosity. *Russ. Geol. Geophys.* 55 (2014), 801–811. doi:10.1016/j.rgg.2014.06.001

Bobrov, A. M., and Baranov, A. A. (2016). The mantle convection model with non-Newtonian rheology and phase transitions: the flow structure and stress fields. *Izv. Phys. Solid Earth* 52 (1), 129–143. doi:10.1134/S1069351316010031

Bobrov, A. M., and Baranov, A. A. (2018). Modeling of moving deformable continents by active tracers: closing and opening of oceans, recirculation of oceanic crust. *Geodyn. Tectonophys.* 9 (1), 287–307. doi:10.5800/GT-2018-9-1-0349

Bobrov, A. M., and Baranov, A. A. (2019). Thermochemical mantle convection with drifting deformable continents: main features of supercontinent cycle. *Pure Appl. Geophys.* 176 (8), 3545–3565. doi:10.1007/s00024-019-02164-w

Brooks, A. N., and Hughes, T. J. R. (1982). Streamline Upwind/Petrov–Galerkin formulations for convection dominated flows with particular emphasis on the incompressible Navier–Stokes equations. *Comput. Methods Appl. Mech. Eng.* 32, 199–259. doi:10.1016/0045-7825(82)90071-8

Brunet, D., and Yuen, D. A. (2000). Mantle plumes pinched in the transition zone. *Earth Planet. Sci. Lett.* 178, 13–27. doi:10.1016/s0012-821x(00)00063-7

Bunge, H. P., Richards, M. A., and Baumgardner, J. R. (1996). Effect of depth-dependent viscosity on the planform of mantle convection. *Nature* 379, 436–438. doi:10.1038/379436a0

Butler, S. L., and Jarvis, G. T. (2004). Stresses induced in continental lithospheres by axisymmetric spherical convection. *Geophys. J. Int.* 157, 1359–1376. doi:10.1111/j.1365-246X.2004.02257.x

Chuvaev, A., Baranov, A., and Bobrov, A. (2020). Numerical modelling of mantle convection in the Earth using cloud technologies. *Comput. Technol.* 25(2), 103–118. doi:10.25743/ICT.2020.25.2.009

Collins, W. J. (2003). Slab pull, mantle convection, and Pangaea assembly and dispersal. *Earth Planet. Sci. Lett.* 205, 225–237. doi:10.1016/S0012-821X(02)01043-9

Condie, K. C. (2004). Supercontinents and superplume events: distinguishing signals in the geologic record Record. *Phys. Earth Planet.* 146, 319–332. doi:10.1016/j.pepi.2003.04.002

Courtillot, V. E., and Renne, P. R. (2003). On the ages of flood basalt events. *Compt. Rend. Geosc.* 335, 113–140. doi:10.1016/S1631-0713(03)00006-3

Donnadieu, Y., Goddéris, Y., Ramstein, G., Nédélec, A., and Meert, J. (2004). A snowball Earth climate triggered by continental break-up through changes in runoff. *Nature* 428 (2004), 303–306. doi:10.1038/nature02408

Fei, Y., Orman, J. V., Li, J., van Westrenen, W., Sanloup, C., Minarik, W., et al. (2004). Experimentally determined postspinel transformation boundary in Mg_2SiO_4 using MgO as an internal pressure standard and its geophysical implications. *J. Geophys. Res.* 109, B02305. doi:10.1029/2003JB002562

Fortin, M., and Fortin, A. A. (1985). Generalization of Uzawa's algorithm for the solution of the Navier–Stokes equations. *Comm. Appl. Numer. Methods* 1, 205–210. doi:10.1002/cnm.1630010504

Gung, Y., Panning, M., and Romanowicz, B. (2003). Global anisotropy and the thickness of continents. *Nature* 422, 707–711. doi:10.1038/nature01559

Gurnis, M. (1988). Large-scale mantle convection and aggregation and dispersal of supercontinents. *Nature* 332, 696–699. doi:10.1038/332695a0

Heron, P. J., and Lowman, J. P. (2011). The effects of supercontinent size and thermal insulation on the formation of mantle plumes. *Tectonophysics* 510, 28–38. doi:10.1016/j.tecto.2011.07.002

Hoffman, P. F. (1991). Did the breakout of laurentia turn gondwanaland inside-out? *Science* 252, 1409–1412. doi:10.1126/science.252.5011.1409

Honda, S., Yoshida, M., Ootorii, S., and Iwase, Y. (2000). The timescales of plume generation caused by continental aggregation. *Earth Planet. Sci. Lett.* 176, 31–43. doi:10.1016/s0012-821x(99)00319-2

Huang, C., Zhang, N., Li, Z. X., Ding, M., Dang, Z., Pourteau, A., et al. (2019). Modeling the inception of supercontinent breakup: stress state and the importance of orogens. *Geochem. Geophys. Geosyst.* 20 (11), 4830–4848. doi:10.1029/2019gc008538

Hughes, T. J. R. (1987). *The finite element method: linear static and dynamic finite element analysis*. New Jersey: Prentice Hall.

Leng, W., and Zhong, S. (2009). More constraints on internal heating rate of the earth's mantle from plume observations. *Geophys. Res. Lett.* 36. doi:10.1029/2008GL036449

Li, Z.-X., Bogdanova, S., Collins, A., Davidson, A., Waele, B., Ernst, R., et al. (2008). Assembly, configuration, and break-up history of Rodinia: a synthesis. *Precambrian Res.* 160, 179–210. doi:10.1016/j.precamres.2007.04.021

Li, Z. X., and Zhong, S. J. (2009). Supercontinent-superplume coupling, true polar wander and plume mobility: plate dominance in whole-mantle tectonics? *Phys. Earth Planet. Inter.* 176, 143–156. doi:10.1016/j.pepi.2009.05.004

Lobkovsky, L., and Kotelkin, V. (2015). The history of supercontinents and oceans from the standpoint of thermochemical mantle convection. *Precambrian Res.* 259, 262–277. doi:10.1016/j.precamres.2015.01.005

Lowman, J. P., and Gable, C. W. (1999). Thermal evolution of the mantle following continental aggregation in 3D convection models. *Geophys. Res. Lett.* 26 (17), 2649–2652. doi:10.1029/1999GL008332

Lowman, J. P., and Jarvis, G. T. (1993). Mantle convection flow reversals due to continental collisions. *Geophys. Res. Lett.* 20, 2087–2090. doi:10.1029/93GL02047

Lowman, J. P., and Jarvis, G. T. (1996). Continental collisions in wide aspect ratio and high Rayleigh number two-dimensional mantle convection models. *J. Geophys. Res.* 101, 25485–25497. doi:10.1029/96JB02568

Lowman, J. P., and Jarvis, G. T. (1999). Effects of mantle heat source distribution on supercontinent stability. *J. Geophys. Res.* 104, 12733–12746. doi:10.1029/1999JB900108

Mao, Y., Zhong, J., and Zhang, J. (2019). The dynamics of an insulating plate over a thermally convecting fluid and its implication for continent movement over convective mantle. *J. Fluid Mech.* 868, 286–315. doi:10.1017/jfm.2019.189

McNamara, A. K., and Zhong, S. (2004). Thermochemical structures within a spherical mantle: superplumes or piles? *J. Geophys. Res. - Solid Earth* 109 (B7), 1–14. doi:10.1029/2003JB002847

Meert, J. G. (2002). Paleomagnetic evidence for a paleo-mesoproterozoic supercontinent columbia. *Gondwana Res.* 5, 207–215. doi:10.1016/S1342-937X(05)70904-7

Mitchell, R. N., Zhang, N., Salminen, J., Liu, Y., Spencer, C. J., Steinberger, B., et al. (2021). The supercontinent cycle. *Nat. Rev. Earth. Environ.* 2, 358–374. doi:10.1038/s43017-021-00160-0

Moresi, L. N., and Gurnis, M. (1996). Constraints on the lateral strength of slabs from three-dimensional dynamic flow models. *Earth Planet. Sci. Lett.* 138, 15–28. doi:10.1016/0012-821X(95)00221-W

Nance, R. D., Murphy, J. B., and Santosh, M. (2014). The supercontinent cycle: a retrospective essay. *Gondwana Res.* 25, 4–29. doi:10.1016/j.gr.2012.12.026

Pelletier, D., Fortin, A., and Camarero, R. (1989). Are FEM solutions of incompressible flows really incompressible. Int. J. Numer. *Methods Fluids* 9, 99–112. doi:10.1002/fld.1650090108

Pesonen, L. J., Mertanen, S., and Veikkolainen, T. (2012). Paleo-Mesoproterozoic supercontinents—a Paleomagnetic view. *Geophysica* 48 (1–2), 5–47.

Phillips, B. R., and Bunge, P. H. (2005). Heterogeneity and time dependence in 3D spherical mantle convection models with continental drift mantle convection models with continental drift. *Earth Planet. Sci. Lett.* 233, 121–135. doi:10.1016/j.epsl.2005.01.041

Phillips, B. R., and Bunge, P. H. (2007). Supercontinent cycles disrupted by strong mantle plumes. *Geology* 35, 847–850. doi:10.1130/g23686a.1

Piper, J. D. A. (2010). Protopangaea: palaeomagnetic definition of Earth's oldest (mid-Archaean-Palaeoproterozoic) supercontinent. *J. Geodyn.* 50 (3), 154–165. doi:10.1016/j.jog.2010.01.0021016/j.jog.2010.01.002

Pisarevsky, S., Elming, S., Pesonen, L., and Li, Z. X. (2014). Mesoproterozoic paleogeography: supercontinent and beyond. *Precambrian Res.* 244, 207–225. doi:10.1016/j.precamres.2013.05.014

Rogers, J. J. W. (1996). A history of continents in the past three billion years. *J. Geol.* 104, 91–107. doi:10.1086/629803

Rogers, J. J. W., and Santosh, M. (2004). *Continents and supercontinents*. New York: Oxford Univ. Press, 308.

Rogers, J. J. W., and Santosh, M. (2009). Tectonics and surface effects of the supercontinent Columbia. *Gondwana Res.* 15, 373–380. doi:10.1016/j.gr.2008.06.008

Schmeling, H., Babeyko, A. Y., Enns, A., Faccenna, C., Funiciello, F., Gerya, T., et al. (2008). A benchmark comparison of spontaneous subduction models—towards a free surface. *Phys. Earth Planet. Interiors* 171, 198–223. doi:10.1016/j.pepi.2008.06.028

Schubert, G., Turcotte, D. L., and Olson, P. (2001). *Mantle convection in the Earth and planets*. Cambridge: Cambridge Univ. Press.

Tan, E., Gurnis, M., and Han, L. (2002). Slabs in the lower mantle and their modulation of plume formation. *Geochem. Geophys. Geosyst.* 3, 1–24. doi:10.1029/2001gc000238

Trubitsyn, V. P., Simakin, A. G., and Baranov, A. A. (2006). The effect of spatial variations in viscosity on the structure of mantle flows. *Izvestiya, Phys. Solid Earth* 42 (1), 1–12. doi:10.1134/S1069351306010010

Yoshida, M. (2010). Temporal evolution of the stress state in a supercontinent during mantle reorganization. *Geophys. J. Int.* 180 (1), 1–22. doi:10.1111/j.1365-246X.2009.04399.x

Yoshida, M. (2013). Mantle temperature under drifting deformable continents during the supercontinent cycle. *Geophys. Res. Let.* 40 (4), 681–686. doi:10.1002/grl.50151

Yoshida, M. (2019). On mantle drag force for the formation of a next supercontinent as estimated from a numerical simulation model of global mantle convection. *Terra nova.* 31, 135–149. doi:10.1111/ter.12380

Yoshida, M., Honda, S., Ootorii, S., and Iwase, Y. (1999). Generation of plumes under a localized high viscosity lid in 3-D spherical shell convection. *Geophys. Res. Lett.* 26 (7), 947–950. doi:10.1029/1999GL900147

Zhang, N., Dang, Z., Huang, C., and Li, Z. X. (2018). The dominant driving force for supercontinent breakup: plume push or subduction retreat? Geos. *Front* 9 (4), 997–1007. doi:10.1016/j.gsf.2018.01.010

Zhang, N., Zhong, S., and McNarmara, A. K. (2009). Supercontinent formation from stochastic collision and mantle convection models. *Gondwana Res.* 15, 267–275. doi:10.1016/j.gr.2008.10.002

Zhang, S., Li, Z.-X., Evans, D. A. D., Wu, H., Li, H., and Dong, J. (2012). Pre-Rodinia supercontinent Nuna shaping up: a global synthesis with new paleomagnetic results from North China. *Earth Planet. Sci. Lett.* 353–354, 145–155. doi:10.1016/j.epsl.2012.07.034

Zhao, G., Sun, M., Wilde, S. A., and Li, S. (2004). A Paleo-Mesoproterozoic supercontinent: assembly, growth and breakup. *Earth-Science Rev.* 67 (1), 91–123. doi:10.1016/j.earscirev.2004.02.003

Zhong, S., Gurnis, M., and Moresi, L. (1998). Role of faults, nonlinear rheology, and viscosity structure in generating plates from instantaneous mantle flow models. *J. Geophys. Res.* 103 (15), 15255–15268. doi:10.1029/98jb00605

Zhong, S., McNamara, A., Tan, E., Moresi, L., and Gurnis, M. (2008). A benchmark study on mantle convection in a 3-D spherical shell using CitcomS. *Geochem. Geophys. Geosyst.* 9, Q10017. doi:10.1029/2008GC002048

Zhong, S., Zhang, N., Li, Z. X., and Roberts, J. H. (2007). Supercontinent cycles, true polar wander, and very long-wavelength mantle convection. *Earth Planet. Sci. Lett.* 261, 551–564. doi:10.1016/j.epsl.2007.07.049

Zhong, S., Zuber, M. T., Moresi, L. N., and Gurnis, M. (2000). Role of temperature-dependent viscosity and surface plates in spherical shell models of mantle convection. *J. Geophys. Res.* 105 (B5), 11063–11082. doi:10.1029/2000JB900003